

Breaking the 800 mV open-circuit voltage barrier in antimony sulfide photovoltaics

Jiacheng Zhou,¹ Xinwei Wang,² Tianle Shi,¹ Lei Wan,¹ Junzhi Ye,³ Zhiqiang Li,⁴ Aron Walsh,^{*2} Robert L. Z. Hoye,^{*3} and Ru Zhou^{*1}

¹ School of Electrical Engineering and Automation, Hefei University of Technology, Hefei 230009, P. R. China

² Department of Materials, Imperial College London, Exhibition Road, London SW7 2AZ, UK

³ Inorganic Chemistry Laboratory, Department of Chemistry, University of Oxford, South Parks Road, Oxford OX1 3QR, United Kingdom

⁴ National-Local Joint Engineering Laboratory of New Energy Photoelectric Devices, College of Physics Science and Technology, Hebei University, Baoding 071002, P. R. China

* Corresponding authors:

a.walsh@imperial.ac.uk (Aron Walsh)

robert.hoye@chem.ox.ac.uk (Robert L. Z. Hoye)

zhouru@hfut.edu.cn (Ru Zhou)

Abstract

Sb_2S_3 is a promising material for low-toxicity, high-stability next-generation photovoltaics. Despite high optical limits in efficiency, progress in improving its device performance has been limited by severe voltage losses. Recent spectroscopic investigations suggest that self-trapping occurs in Sb_2S_3 , limiting the open-circuit voltage (V_{OC}) to a maximum of approximately 800 mV, which is the level the field has asymptotically approached. In this work, we surpass this voltage barrier through reductions in the defect density in Sb_2S_3 thin films by modulating the growth mechanism in chemical bath deposition using citrate ligand additives. Deep level transient spectroscopy identifies two deep traps 0.4–0.7 eV above the valence band maximum, and, through first-principles calculations, we identify these to likely be S vacancies, or Sb on S anti-sites. The concentrations of these traps are lowered by decreasing the grain boundary density from $1114 \pm 52 \text{ nm } \mu\text{m}^{-2}$ to $585 \pm 10 \text{ nm } \mu\text{m}^{-2}$, and we achieve a V_{OC} of 824 mV, the record for Sb_2S_3 solar cells. This work addresses the debate in the field around whether Sb_2S_3 is limited by defects or self-trapping, showing that it is possible to improve the performance towards the radiative limit through careful defect engineering.

Keywords: Sb_2S_3 solar cells, open-circuit voltage, chemical bath deposition, defects

Introduction

Thin film photovoltaics are important alternatives to silicon-based solar cells because of their high performance, lower materials use, compatibility with fabrication into larger-area modules, and lower levelized cost of electricity^{1,2}. As representatives, CdTe and Cu(In,Ga)(S,Se)₂ (CIGS) have achieved remarkable certified power conversion efficiencies (PCEs) of 23.1% and 23.6% at the laboratory scale, respectively³. Nevertheless, the use of toxic (i.e., Cd) and scarce (i.e., In, Ga) elements impede their widespread deployment on the multi-terawatt level. The ongoing development of highly efficient, cost-effective, earth-abundant solar cells that have low environmental impact and carbon dioxide equivalent (CO₂eq) footprint has led to the continuous emergence of light-harvesting materials for next-generation thin film photovoltaics, including Sb₂S₃, Sb₂Se₃, SnS, GeSe, CuSbS₂, CuSbSe₂, Cu₂ZnSnS₄, Cu₂ZnSn(S,Se)₄^{4, 5, 6, 7, 8, 9, 10, 11, 12}. Antimony chalcogenides are at the forefront of emerging sustainable photovoltaic materials due to their excellent electronic and optical properties^{4, 7, 13, 14, 15, 16}. This material system exhibits high absorption coefficient ($>10^5$ cm⁻¹ in the visible range), tunable bandgap (1.1-1.7 eV), decent charge-carrier mobility in thin films (~ 10 cm² V⁻¹ s⁻¹), and excellent thermal and environmental stability. Additionally, the quasi-one-dimensional (quasi-1D) crystal structure that comprises numerous [Sb₄S₆]_n or [Sb₄Se₆]_n ribbons enables efficient charge-carrier transport in the out-of-plane direction if the crystal orientation of antimony chalcogenide thin films can be effectively controlled^{17, 18}. Antimony chalcogenide solar cells have recently exceeded a 10% efficiency benchmark based on Sb₂(S,Se)₃ absorbers, making them competitive in the emerging thin film photovoltaics field^{5, 7, 13, 19}.

The binary compound semiconductor Sb₂S₃ possesses a bandgap in the range of 1.7-1.8 eV, close to the optimal value for indoor photovoltaics (IPVs) and top-cells for silicon-based tandem photovoltaics^{20, 21, 22}. According to the Shockley-Queisser (S-Q) detailed balance limit for the single p-n junction, under standard one-sun (AM1.5G, 100 mW cm⁻²) illumination, the theoretical device parameters achievable with a 1.70 eV bandgap light-harvester are an open-circuit voltage (V_{OC}) of 1.402 V, a short-circuit

current density (J_{SC}) of 22.46 mA cm⁻², a fill factor (FF) of 91%, and a power conversion efficiency (PCE) of 28.64%^{23, 24}. During the past decade, Sb₂S₃ solar cells have made notable strides in performance. However, the most efficient Sb₂S₃ solar cells reported thus far (8.32% PCE) still falls far behind the detailed-balance limit²⁵. Like other emerging light absorbers, the performance of Sb₂S₃ solar cells is primarily limited by the large V_{OC} deficit². At present, the V_{OC} of Sb₂S₃ solar cells has stagnated in the range of 550-770 mV for decades, much smaller than other photovoltaic devices based on absorbers with similar or smaller bandgaps, such as CdTe, GaAs, CIGS, InP, CH₃NH₃PbI₃ or crystalline-Si, as summarized in Fig. 1a^{1, 26}. To date, the V_{OC} of 753 mV obtained in the highest-efficiency Sb₂S₃ device at present is only 53.7% of the radiative limit, suffering from a V_{OC} deficit greater than 600 mV²⁵. Here the V_{OC} deficit is defined as $V_{OC}^{SQ} - V_{OC}$, where V_{OC}^{SQ} is the S-Q limit V_{OC} , evaluated using the empirical equation $V_{OC}^{SQ} = 0.932 \times E_g/q - 0.167 V$ (E_g is the bandgap of absorber; Fig. 1a)²⁷. Overcoming the V_{OC} bottleneck is critical to ensure that progress with Sb₂S₃ photovoltaics does not stagnate.

The origin of the V_{OC} bottleneck of Sb₂S₃ solar cells remains under debate, with two perspectives illustrated in Fig. 1b. One explanation proposed by Yang et al. is self-trapping of photoexcited charge-carriers, which sets an upper limit to the maximum V_{OC} (~800 mV) and PCE (~16.00%) for Sb₂S₃ solar cells²⁸. The proposed mechanism involves excitation from the ground state (GS) to excited state (ES), before relaxing to self-trapped exciton (STE) states due to electron-phonon coupling, leading to energy losses and reductions in the quasi-Fermi level splitting. This mechanism is linked to their experimental observation of a 600 meV red-shift in photoluminescence (PL) compared to the optical bandgap, along with polarized light emission from Sb₂S₃ single crystals. A similar carrier self-trapping effect has also been proposed for Sb₂Se₃²⁹. If self-trapping were indeed limiting the performance of these materials, this places a fundamental limitation on the performance below the radiative limit, since carrier localization takes place intrinsically, even in a defect-free material. In contrast, first-principles analysis of electron-lattice interactions and charge-carrier mobility suggest

that the low effective masses in Sb_2S_3 lead to band-like transport in these materials, and the key limiting factor for V_{OC} is defect-mediated rather than self-trapping³⁰. Several experimental studies have linked the high V_{OC} deficit in Sb_2S_3 solar cells to a complex set of defects with deep levels^{27, 31, 32}. For example, we previously showed that lowering the defect density in Sb_2S_3 by reducing the grain boundary (GB) density results in an increase in device performance, including improvements in V_{OC} ¹⁴. In-depth investigations combining theory and experiments are needed to resolve this debate to understand whether Sb_2S_3 is fundamentally limited in performance, or has hope still of further improvements towards the radiative limit. But beyond mechanistic studies, it is essential to demonstrate if devices surpassing the limits expected from self-trapping could be realized.

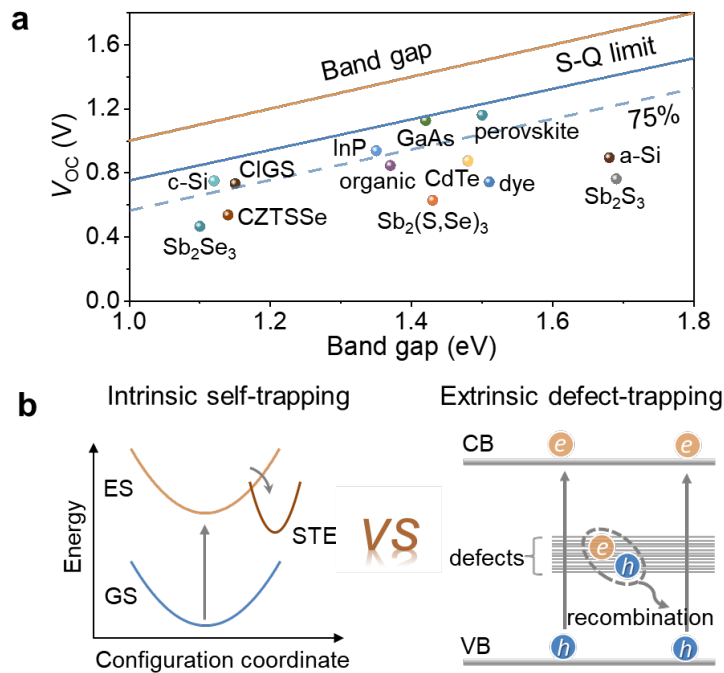


Fig. 1 | Proposed mechanisms for factors limiting the open-circuit voltage of Sb_2S_3 solar cells.

a Reported V_{OC} values of well-developed thin film solar cells, as well as the most efficient antimony chalcogenides^{1, 26}. Theoretical S-Q limit of V_{OC} as a function of band gap (solid blue line) and 75% of the limit (dashed line) are highlighted. **b** Qualitative adiabatic potential energy curve (left) showing the self-trapping effect: photoexcitation from ground state (GS) to excited state (ES) evolves into a self-trapped exciton (STE) state from lattice distortions and losing substantial energy.

Schematic (right) showing the defect-trapping effect: the photoexcited electrons and holes suffer from charge recombination at the defects.

In this work, we developed Sb_2S_3 solar cells with the V_{OC} breaking the 800 mV barrier by using a complexing agent-mediated chemical bath deposition (CBD) method, which enables the deposition of high-quality Sb_2S_3 thin films with GB density approximately halved. The reduced impact of defects for Sb_2S_3 films, confirmed by deep-level transient spectroscopy (DLTS) characterization and first-principles calculations, is revealed to contribute to the smaller V_{OC} deficit. The obtained V_{OC} of 824 mV is the current record for antimony chalcogenide solar cells. The trap-limited V_{OC} and PCE as well as the radiative limit of Sb_2S_3 solar cells was also assessed by computations. This work reveals that defect-mediated recombination is a key limitation to the device V_{OC} and PCE, and the low performance of Sb_2S_3 photovoltaics is surmountable through defect engineering to reach towards the radiative limit.

Results

Performance of planar Sb_2S_3 solar cells

In this work, a modified CBD method was explored to deposit large-grained Sb_2S_3 absorber films. It is known that additive engineering in CBD solutions by incorporating reasonable complexing agents is an effective strategy to regulate the film properties (such as surface morphology, GB density, defect density, carrier concentration, etc.) via the facile modulation of *in-situ* chemical environment for film deposition^{23, 33}. Here, potassium antimony tartrate ($\text{C}_4\text{H}_4\text{KO}_7\text{Sb}\cdot 0.5\text{H}_2\text{O}$, APT) and sodium thiosulfate ($\text{Na}_2\text{S}_2\text{O}_3\cdot 5\text{H}_2\text{O}$, STS) were employed as the Sb source and S source, respectively, and a small amount of sodium citrate (SC) was used as a complexing additive in the precursor solution to manipulate the nucleation and growth kinetics of Sb_2S_3 films. For the convenience of description, the Sb_2S_3 samples obtained with the SC concentrations of 1 mM, 2 mM, 4 mM, and 8 mM in the precursor solutions are labeled as 1mM-SC, 2mM-SC, 4mM-SC, and 8mM-SC, respectively. The planar n-i-p device configuration

used is FTO/SnO₂/CdS/Sb₂S₃/Spiro-OMeTAD/Au (Fig. 2a). Here Sb₂S₃ is the absorber, and SnO₂/CdS and Spiro-OMeTAD act as the electron transport layer (ETL) and hole transport layer (HTL), respectively. The detailed fabrication processes of Sb₂S₃ solar cells are illustrated in Supplementary Fig. 1. The photovoltaic parameters of Sb₂S₃ solar cells, each based on 12 cells, including V_{OC} , J_{SC} , FF, and PCE, achieved under one-sun illumination (AM1.5G, 100 mW cm⁻²), are summarized in the box charts of Fig. 2b. The corresponding device parameters are summarized in Table 1. As shown, these devices exhibit excellent performance and repeatability. The device PCE increases at first and then decreases with the increase of the SC concentration in the CBD precursor solution. The control Sb₂S₃ devices obtained without the use of SC deliver an average PCE of 6.23%, whereas the average PCE is increased to 7.46% for the 4mM-SC devices. The current density-voltage (J - V) curves of best-performing control and 4mM-SC Sb₂S₃ solar cells are given in Fig. 2c. The control device yields a V_{OC} of 787 mV and a PCE of 6.42%; the 4mM-SC device affords a V_{OC} of 817 mV and a PCE of 7.67%. That is, the incorporation of 4mM SC leads to the relative PCE increasing by nearly 20% compared to the control device. The external quantum efficiency (EQE) spectra of the control and 4mM-SC solar cells, as given in Fig. 2d, reveal that both devices present broad light responses ranging from 350 to 750 nm. Compared to the control device, the 4mM-SC device exhibits enhanced EQE, with the value exceeding 90% at around 530 nm. The obtained integrated J_{SC} from EQE spectra are 14.95 and 16.13 mA cm⁻² for the control and 4mM-SC devices, respectively, consistent with that obtained from J - V curves (within 5% deviation). Fig. 2e summarizes the V_{OC} evolution of well-developed planar and sensitized Sb₂S₃ solar cells (detailed in Supplementary Table 1). As shown, the V_{OC} presents continuous enhancements over the past decade, especially for the planar configuration. However, the V_{OC} shows relatively slow growth in contrast to the rapid PCE increase. To the best of our knowledge, the V_{OC} of 824 mV obtained for the 4mM-SC device is the highest value reported for Sb₂S₃ solar cells. Interestingly, this V_{OC} value is beyond the predicted limit for Sb₂S₃ if it had self-trapping²⁸. We also found that CBD-processed Sb₂S₃ photovoltaics exhibited excellent environmental stability. The unencapsulated 4mM-SC Sb₂S₃ solar cell retained 97.4% of its initial efficiency

after 30 days of storage in the dark under ambient temperature in a cabinet with 15% relative humidity (Supplementary Fig. 2).

Moreover, it is known that the bandgap of Sb_2S_3 is ideal for IPVs³³. Thus we further measured the IPV performance of Sb_2S_3 solar cells under illumination from white light emitting diodes (WLEDs) with a correlated color temperature (CCT) of 3000 K, and details of the spectral irradiance, the stability of light source, and indoor photovoltaic device performance for 4 mM-SC are shown in Supplementary Fig. 3 and 4, along with Supplementary Table 2. The short-circuit current density is approximately linearly proportional to the light intensity, while the V_{OC} and FF increase approximately logarithmically with the light intensity. As a result, the highest Sb_2S_3 IPV efficiency is under 1000 lux, with a state-of-the-art indoor PCE of 18.56%. This exceeds our previous report of Sb_2S_3 IPVs (17.6% indoor PCE), and is comparable with the current state-of-the-art for not just Sb_2S_3 , but also other Sb- and Bi-based solar absorbers^{33, 34, 35}. The loss in V_{OC} from 1000 lux to 200 lux in the 4 mM-SC IPVs is 61 mV, which is low compared to other established and emerging IPVs³⁶.

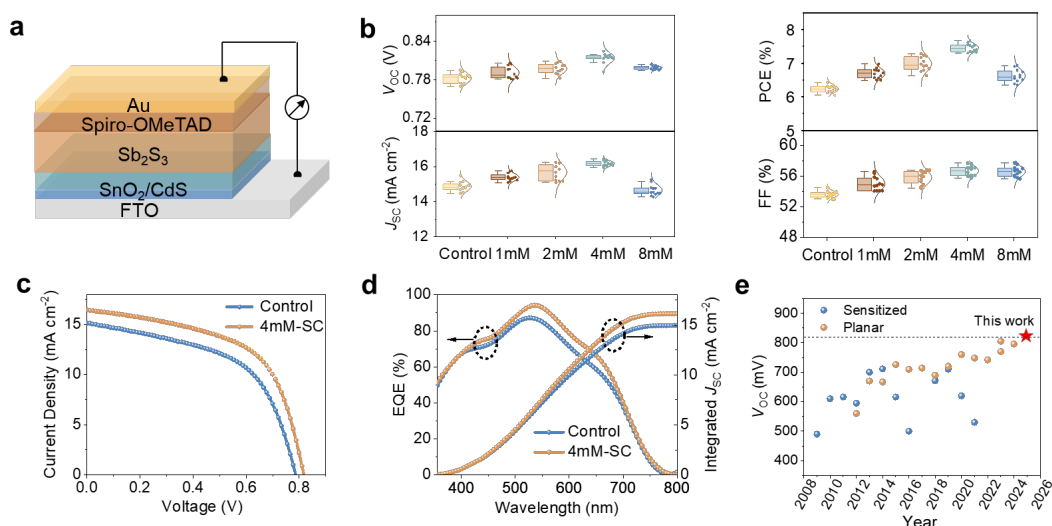


Fig. 2 | Photovoltaic performance of planar Sb_2S_3 thin film solar cells. **a** The planar configuration of FTO/ SnO_2 / CdS / Sb_2S_3 /Spiro-OMeTAD/Au used in this work. **b** Statistics of the performance parameters of Sb_2S_3 solar cells obtained without (i.e., control) and with the addition of different SC concentrations. **c** Current density-voltage (J - V) curves of best-performing control and 4mM-SC

Sb₂S₃ solar cells, measured under one-sun (AM 1.5G, 100 mW cm⁻²) illumination. **d** External quantum efficiency (EQE) spectra of control and 4mM-SC Sb₂S₃ solar cells. **e** Evolution in the record V_{OC} values of planar and sensitized Sb₂S₃ solar cells.

Table 1 | Photovoltaic parameters of the control and SC-Sb₂S₃ solar cells, measured under one-sun (AM 1.5G, 100 mW cm⁻²) illumination. Format: average \pm standard deviation (best value)

Device	V_{OC} (mV)	J_{SC} (mA cm ⁻²)	FF (%)	PCE (%)
Control	782 \pm 8	14.87 \pm 0.2	53.60 \pm 0.42	6.23 \pm 0.11
	(795)	(15.15)	(53.90)	(6.42)
1mM-SC	791 \pm 10	15.40 \pm 0.21	55.02 \pm 0.90	6.70 \pm 0.15
	(806)	(15.76)	(56.58)	(6.98)
2mM-SC	797 \pm 8	15.69 \pm 0.45	55.85 \pm 0.86	6.98 \pm 0.21
	(807)	(16.23)	(56.75)	(7.29)
4mM-SC	814 \pm 8	16.18 \pm 0.15	56.68 \pm 0.67	7.46 \pm 0.12
	(824)	(16.44)	(57.70)	(7.67)
8mM-SC	799 \pm 3	14.65 \pm 0.31	56.60 \pm 0.67	6.62 \pm 0.19
	(803)	(15.26)	(56.99)	(6.93)

Characterization of CBD-processed Sb₂S₃ films

Fig. 3a and b shows top-view scanning electron microscopy (SEM) images of Sb₂S₃ thin films prepared without the SC additive (i.e., the control sample) and with different concentrations of 4 mM SC, respectively. It can be seen that, the control Sb₂S₃ film sample displays grain sizes smaller than 3 μ m based on the long diameters of polygon-shaped grains, consistent with that reported for CBD-processed Sb₂S₃ films in the literature⁴. With the addition of SC, the grain size of Sb₂S₃ films involves an obvious increase, with many Sb₂S₃ grains exceeding 5 μ m. Top-view SEM images of Sb₂S₃ films prepared with the use of other SC concentrations are provided in Supplementary Fig. 5. The increase in grain size is accompanied by a decrease in GB density, which is defined as the GB length per unit area. Fig. 3a gives the dependence of GB density on

the SC concentration for different Sb_2S_3 films. As shown, the GB density on the surface of Sb_2S_3 films decreases from $1114 \pm 52 \text{ nm } \mu\text{m}^{-2}$ for the control sample to 666 ± 17 , 641 ± 16 , 586 ± 11 and $901 \pm 31 \text{ nm } \mu\text{m}^{-2}$ for 1mM-SC, 2mM-SC, 4mM-SC and 8mM-SC film samples, respectively. In polycrystalline films, the recombination losses are largely caused by GBs where dangling or wrong bonds proliferate¹⁴. Hence, the performance could be increased for polycrystalline absorbers with reduced GB density.

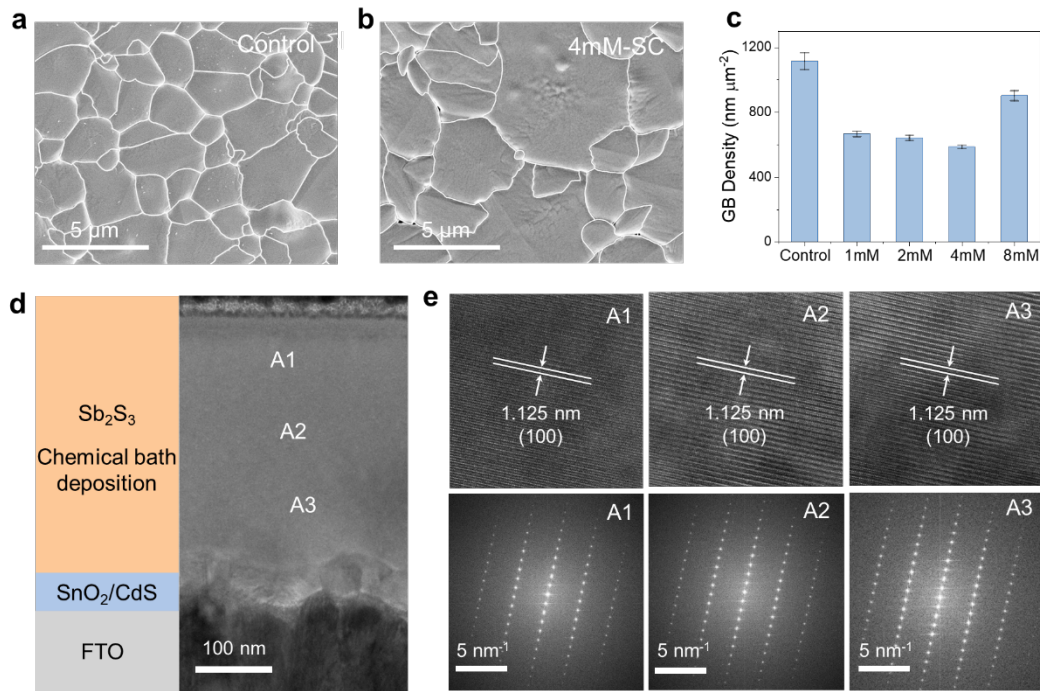


Fig. 3 | Morphological properties of highly crystalline Sb_2S_3 thin films. **a,b** Top-view scanning electron microscopy (SEM) images of Sb_2S_3 films prepared without (i.e., control) and with the addition of 4 mM SC. The GBs are highlighted to clearly show the changes in GB density. **c** Change in GB density with SC concentration in the precursor solution. Three samples were used to determine the mean GB density values shown, and the error bars denote the standard deviation. **d** Cross-sectional transmission electron microscopy (TEM) image of 4mM-SC Sb_2S_3 sample deposited on FTO/SnO₂/CdS substrate. **e** High-resolution TEM images performed at points A1, A2, and A3 (see part D), and corresponding fast Fourier transform (FFT) patterns.

To further confirm the single-crystalline nature of individual Sb_2S_3 grains observed from SEM images, we performed characterization based on the Sb_2S_3 lamella sample

(4mM-SC film) prepared by focused ion beam (FIB). The cross-sectional transmission electron microscopy (TEM) image (Fig. 3b) indicates that the Sb_2S_3 sample is compact and composed of large grains spanning the thickness of the Sb_2S_3 film. Fig. 3c shows the high-resolution TEM (HRTEM) images of three arbitrarily selected points A1, A2, and A3, as labeled in Fig. 3b. As shown, points A1, A2, and A3 share identical crystallographic orientations, revealing that the crystal planes extend from the top to the bottom of the Sb_2S_3 film. Lattice fringes with interplanar spacings of 1.125 nm, corresponding to the (100) plane in orthorhombic Sb_2S_3 , were identified¹⁴. The nearly identical fast Fourier transform (FFT) patterns of HRTEM images of points A1, A2, and A3 further confirm that the individual microstructural units bounded by GBs are indeed single crystals. The cross-sectional elemental mapping images (Supplementary Fig. 6) indicate the uniform distribution of Sb and S across the absorber layer and the conformal growth of Sb_2S_3 on top of the CdS buffer layer. The HRTEM image at the CdS/ Sb_2S_3 interface (Supplementary Fig. 7) reveal the lattice fringes assigned to Sb_2S_3 and CdS¹⁴. The results confirmed that Sb_2S_3 films with large single-crystalline grains could be easily produced via CBD.

X-ray diffraction (XRD) patterns of Sb_2S_3 films (Supplementary Fig. 8a) show that the diffraction peaks can be well indexed to orthorhombic Sb_2S_3 (JCPDS #42-1393)²³. The diffraction peaks of Sb_2S_3 films reveal negligible shifts with the use of SC, indicating that the SC additive could not be incorporated into the Sb_2S_3 lattice or interstitial sites. We further calculated the texture coefficient (TC) of the dominant ($hk0$) and ($hk1$) planes to quantify the degree of preferred orientation of Sb_2S_3 films (Supplementary Fig. 8b). The addition of SC does not cause significant changes to the film orientation. Additionally, compared to the control film, the SC- Sb_2S_3 films involve a gradual reduction in the dominant diffraction peak intensities, such as (120), (130), (211), (221), with the increase in the SC concentration. This should be closely associated with the decrease in the film thickness, as reflected in the cross-sectional SEM images of Sb_2S_3 films (Supplementary Fig. 9). As shown, the film thickness gradually decreases from 506 ± 26 nm for the control sample to 394 ± 10 nm, 347 ± 28

nm, 318 ± 15 nm and 116 ± 32 nm for 1mM-SC, 2mM-SC, 4mM-SC, and 8mM-SC samples, respectively.

The two-dimensional (2D) morphology spatial maps of atomic force microscopy (AFM) characterization (Supplementary Fig. 10) confirm the 4mM-SC film shows larger grain sizes with fewer GBs than the control. Furthermore, the addition of SC leads to a reduction in the root-mean-square roughness from 21.9 nm (the control sample) to 16.3 nm (the 4mM-SC sample). The reduced surface roughness of the absorber films would favor the formation of an improved heterojunction between Sb_2S_3 and solution-processed HTL on top. Conductive-atomic force microscopy (c-AFM) images, with the corresponding morphology and current maps (Supplementary Fig. 11) reveal that, compared to the control sample, the 4mM-SC films have more uniform and slightly enhanced electrical conductivity over the $5 \times 5 \mu\text{m}^2$ area measured. The reduced fluctuation of the current intensity for the 4mM-SC Sb_2S_3 film should be conducive to the local photocurrent generation and collection, which might effectively suppress charge-carrier recombination at GBs³⁷. Moreover, the GBs of Sb_2S_3 grains generally involve lower conductivity than grain interiors, suggesting the inefficient carrier separation and transport derived from defects at the GBs³⁸. We further performed Kelvin probe force microscopy (KPFM) to map the surface potential of Sb_2S_3 films (Supplementary Fig. 12), which reveals a higher surface potential for the 4mM-SC film in contrast to the control sample. Regarding that an increase in the surface potential corresponds to a reduced work function (WF) (i.e., closer to the vacuum level), the smaller WF for the 4mM-SC sample implies the upshift of Fermi levels^{37, 39}. This is consistent with the band structure of Sb_2S_3 solar cells, obtained from ultraviolet photoelectron spectroscopy (UPS) spectra (Supplementary Fig. 13) and absorption spectra (Supplementary Fig. 14). Compared to the control Sb_2S_3 film, the Fermi level of SC- Sb_2S_3 is shifted up towards conduction band (CB), indicating an increase in the electron carrier concentration for n-type Sb_2S_3 .

We further investigate the underlying mechanism that could explain the impact of the SC complexing agent on Sb_2S_3 film properties. For the CBD of Sb_2S_3 films, the substrate is exposed to soluble precursors which react or decompose to form the desired

film materials⁴⁰. From the perspective of nucleation and growth, an intricate balance of growth parameters is necessary to achieve high-quality films. The formation of Sb₂S₃ grains typically involves nucleation and growth, which are greatly influenced by the chemical environment of precursor solutions^{41, 42, 43}. We measured the contact angles of the substrate treated by precursor solutions with different SC concentrations and further analyzed the ratio of the free energies of homogeneous and heterogeneous nucleation as a function of the contact angle (Supplementary Fig. 15a, b, detailed in Supplementary Note 1). The results demonstrate that the incorporation of SC would promote the heterogeneous nucleation of Sb₂S₃ on the substrate. Our proposed mechanism is schematically illustrated in Supplementary Fig. 15c. We suggest that adding SC changes the growth mode of Sb₂S₃ films from cluster deposition to ion-by-ion deposition. For the pristine CBD solution without the use of SC, the strong complexation effect of ATP would cause the formation of many aggregates in the precursor, which serve as homogeneous nucleation centers for Sb₂S₃⁴⁴. These small clusters created within the solution further migrate and adhere onto the substrate surface, resulting in the deposition of Sb₂S₃ films in the cluster mechanism. For the ion-by-ion deposition mechanism, the complexing agent enables the slow release of free metal ions to directly react with anions onto the substrate in a more controlled manner, being capable of forming well-textured crystalline or even monocrystalline films⁴⁰. Ion-by-ion deposition therefore promotes heterogeneous nucleation on the substrate and suppresses homogeneous nucleation in the precursor solution, similar to the scenario demonstrated for the CBD of other metal chalcogenide thin films, such as ZnS⁴⁵. High-density small nuclei formed on the substrate would further coalesce into a large-grained Sb₂S₃ film during the CBD process. Hence the formation of stable citrate-complexed Sb³⁺ succeeds to control the nucleation and growth rate of Sb₂S₃, contributing to the deposition of large-grained Sb₂S₃ films. In fact, previous studies also demonstrated that films grown by ion-by-ion deposition are usually associated with larger crystalline size compared to those grown by cluster deposition⁴⁰. Additionally, the decrease in the release rate of Sb³⁺ further reduces the film thickness, explaining the thickness evolution of Sb₂S₃ films with the addition of SC. Apart from the complexation of citrate,

we speculate that pH might be another critical factor influencing the deposition of Sb_2S_3 films. The influence of pH on the deposition of Sb_2S_3 films is further discussed in Supplementary Note 2. It is revealed that, besides the complexation of Sb^{3+} with citrate, the increase in pH should also contribute to the reduction in the deposition rate. However, controlling pH alone does not lead to increases in PCE as high as with the addition of SC (Supplementary Fig. 16). The results imply that the increase in PCE for SC- Sb_2S_3 solar cells should be mainly associated with the complexation Sb^{3+} with citrate which causes the evolution in the morphology of Sb_2S_3 absorber films.

Defect physics and charge-carrier transport properties

Understanding the nature of active defects in Sb_2S_3 is necessary to design strategies to minimize their impact. DLTS is a powerful technique offering insights into the trap energy, defect type and defect concentration in thin film solar cells^{46, 47, 48, 49}. DLTS utilizes the transient capacitance of a p-n junction at varying temperatures as a probe to reflect the changes in the charge state of a deep defect center. The traps within the device are filled with carriers by applying a voltage pulse, which in turn alters the capacitance associated with the p-n junction. Fig. 4a, b illustrate the mechanism of DLTS measurements. Here we take the minority traps (i.e., electron traps in p-type semiconductors) as an example to show the change of transient capacitance caused by electron capture and emission. For a p-n junction, when a constant reverse bias (U_R) is applied, a stable space charge region (SCR) is established, corresponding to a stable capacitance (C_R). If an extremely short fill voltage pulse (U_P) is applied as a perturbation, the SCR width and capacitance change due to the injection of majority carriers into the SCR, causing the traps to be filled during this process. Once the voltage pulse is removed, the SCR and capacitance cannot immediately recover to their original state. This delayed recovery occurs because the trapped carriers are emitted to the CB or valence band (VB) at a specific rate, rather than instantaneously. Consequently, a transient capacitance change over time is observed, and the dynamic capacitance can be described using the Eq. 1⁴⁹:

$$C(t) = C_R + \Delta C * \exp\left(-\frac{t}{\tau_e}\right) \quad (1)$$

where ΔC is the amplitude of the transient capacitance and τ_e is the emission time constant, which is the reciprocal of emission rate, expressed by the Eq. 2⁵⁰:

$$\tau_e = \frac{t_2 - t_1}{\ln\left(\frac{t_2}{t_1}\right)} \quad (2)$$

As ΔC and τ_e vary with temperature, a sequence of the transient capacitance is further collected at various temperatures. The capacitance changes within a time window ($\Delta C = C_{t2} - C_{t1}$) vs. the different temperatures (T) are sampled as the DLTS signals. For the analysis of DLTS measurements, the activation energy (E_a) and capture cross-section (σ) of defects are determined from the Arrhenius plots using Eqs. 3 and 4 6:

$$\ln(\tau_e v_{th,n} N_C) = \frac{E_C - E_T}{k_B T} - \ln(X_n \sigma_n) \quad (3)$$

$$\ln(\tau_e v_{th,p} N_V) = \frac{E_T - E_V}{k_B T} - \ln(X_p \sigma_p) \quad (4)$$

where τ_e denotes the emission time constant, E_C , E_V , and E_T are the CB minimum (CBM), valance band maximum (VBM), and defect energy level, respectively. $v_{th,n}$ and $v_{th,p}$ indicate the thermal velocities for electron and hole traps, respectively. X_n and X_p are the entropy factor for hole and electron, respectively. N_C and N_V represent the density of states of CB and VB, respectively. σ_n and σ_p represent the capture cross-section of electron and hole traps, respectively. T and k_B are the temperature and Boltzmann constant, respectively. E_a is calculated using $E_C - E_T$ for electron trap and $E_T - E_V$ for hole trap. E_a can be obtained from the slope of Arrhenius plots through linear regression. σ can be extracted from the intersection of a line with the y-axis. The trap density (N_T) can be obtained using Eq. 5⁴⁹:

$$N_T = 2N_S \Delta C / C_R \quad (5)$$

where N_S represents the shallow donor/acceptor concentration in absorber films, C_R and ΔC represent the capacitance at reverse bias in equilibrium and the amplitude of capacitance transient, respectively. In particular, the trap type is determined by the ΔC . If $\Delta C < 0$ and the DLTS signal peaks are negative, they correspond to the minority-carrier trap; in contrast, they are majority-carrier traps^{49, 50, 51}.

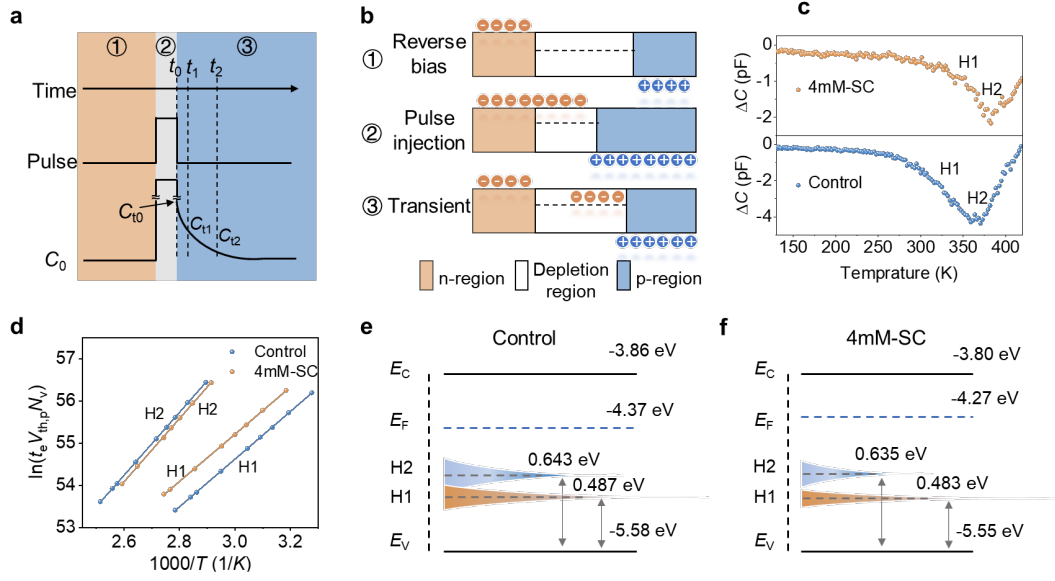


Fig. 4 | DLTS characterization of defect physics in Sb_2S_3 solar cells. **a** Schematic illustration of the mechanism of DLTS measurement. Here we take the minority traps (i.e., electron traps in p-type semiconductors) as an example to illustrate the change of transient capacitance caused by electron capture and emission. **b** The variation of depletion width and the process of carriers being trapped and emitted during the measurement. **c** DLTS signals from the control and 4mM-SC Sb_2S_3 solar cells. **d** Arrhenius plots derived from DLTS signals. Data points are achieved by calculating internal transients included in DLTS signals with the discrete Laplace transform, and the solid lines are corresponding linear fits. **e, f** Schematic of band edge positions and defect levels of the control and 4mM-SC Sb_2S_3 , respectively, including CBM (E_c) and VBM (E_v), Fermi level (E_f) and defect energy levels (H1, H2), relative to the vacuum level.

Table 2 | Defect characteristic parameters, including trap energy level (E_T), cross section (σ), and trap concentration (N_T), obtained using DLTS characterization in the control and 4mM-SC Sb_2S_3 solar cells.

Devices	Trap	E_T [eV]	σ [cm^2]	N_T [cm^{-3}]	$\sigma \times N_T$ [cm^{-1}]
Control	H1	$E_V + 0.487$	4.43×10^{-17}	2.42×10^{15}	0.107
	H2	$E_V + 0.643$	7.35×10^{-16}	1.39×10^{15}	1.020
4mM-SC	H1	$E_V + 0.483$	2.08×10^{-17}	9.14×10^{14}	0.019
	H2	$E_V + 0.635$	6.62×10^{-16}	1.03×10^{15}	0.682

As shown in Fig. 4c, the control device and 4mM- device both present two negative DLTS signal peaks in the high temperature region, denoted as H1 and H2, due to the effect of multiple minority-carrier traps, i.e., hole defects in n-type Sb_2S_3 films⁶. The defect characteristic parameters, including trap energy (E_T) and capture cross section (σ), and trap concentration (N_T), can be extracted from the linear fittings of the Arrhenius plots as given in Fig. 4d, with the results summarized in Table 2. Both devices share similar types of deep levels with densities of approximately 10^{15} cm^{-3} . The trapping behavior can be quantified by using the thermal trapping rate (C_{trap}), expressed by Eq. 6⁴⁸:

$$C_{\text{trap}} = 1/\tau_{\text{trap}} = v\sigma N_T \quad (6)$$

where τ_{trap} is the carrier lifetime associated with the trap-assisted Shockley-Read-Hall (SRH) recombination, which is inversely proportional to $\sigma \times N_T$, and v is the thermal velocity of charge related to the intrinsic charge transport feature of semiconductors. The values of $\sigma \times N_T$ for the control and 4mM-SC devices are summarized in Table 2. Compared to H1, H2 dominates the charge trapping in absorber films with a larger $\sigma \times N_T$ value and greater energy depth. Compared to the control device, the $\sigma \times N_T$ value for the H2 defect in 4mM-SC Sb_2S_3 is decreased. The band edge position and defect levels are illustrated in Fig. 4e, f, with the hole traps situated 0.4-0.7 eV above the VBM. Since the trap energy reflects the difficulty of charge emission from the traps, the H1 and H2 defects located at more than 0.3 eV above the VB would trap carriers without re-emission and act as recombination centers due to their high ionization energy, contributing to severe non-radiative recombination. In particular, the deep-level defects would cause a fluctuation in the bandgap and bring band tail states within the bandgap, giving rise to a further V_{OC} loss. Hence the 4mM-SC Sb_2S_3 film with reduced defect density is suggested to effectively suppress charge recombination in solar cells.

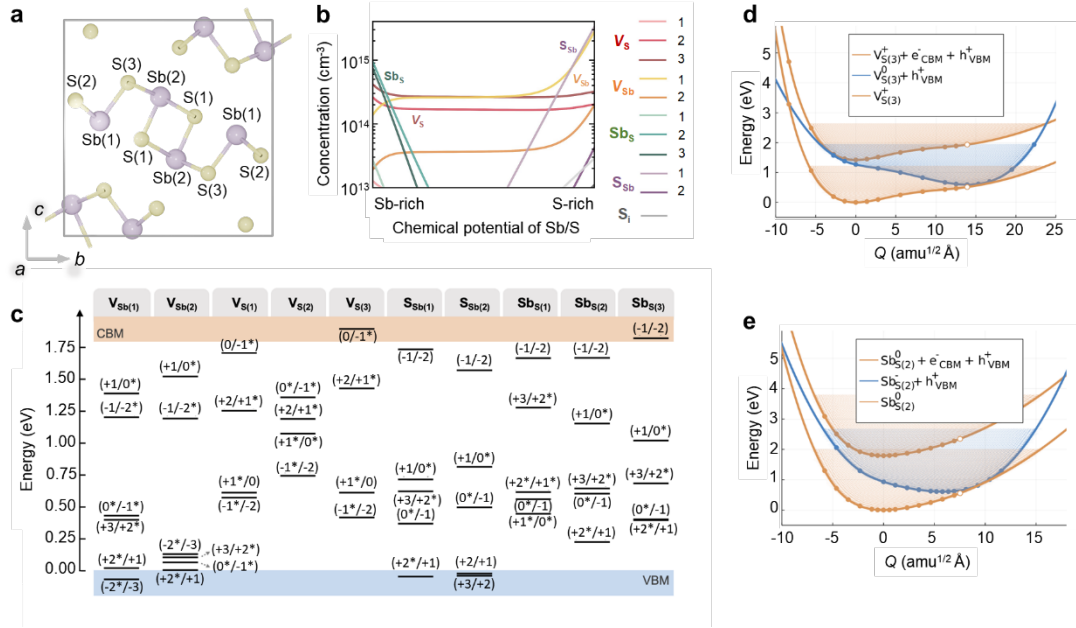


Fig. 5 | First-principles calculations to identify defect species. **a** Illustration of a $[Sb_4S_6]_n$ unit in the Sb_2S_3 crystal structure. **b** Calculated equilibrium defect concentration at 300 K in Sb_2S_3 crystals grown at 643 K as a function of growth conditions based on the defect energies reported in Ref.⁵². The numbers in the legend represent different inequivalent sites. **c** Calculated charge transition levels of intrinsic point defects with high concentrations under Sb-rich conditions in Sb_2S_3 . Metastable charge states are marked with asterisks (*). The Fermi level is referenced to the valence band maximum (VBM). Dashed grey lines indicate trap levels in control and 4mM-SC Sb_2S_3 devices, determined by DLTS. **d, e** 1D configuration coordinate diagram for charge transitions between $V_{S(3)}^+$ and $V_{S(3)}^0$ as well as $S_{Sb(2)}^0$ and $S_{Sb(2)}^-$. Q represents the generalized configuration coordinate, which describes the collective atomic displacement along the reaction pathway during charge transition. The equilibrium structures of $V_{S(3)}^+$ and $S_{Sb(2)}$ are set as references with $Q = 0$ amu^{1/2}Å and total energy $E = 0$ eV. Solid circles are data points obtained by DFT calculations and used for fitting, while hollow circles are discarded for fitting due to charge delocalization. Solid lines represent best fits to the data.

To identify the defect species, we performed first-principles calculations combined with a global searching strategy, implemented in the doped⁵³ and ShakeNBreak packages⁵⁴, to systematically explore all symmetry-inequivalent configurations of intrinsic point defects in Sb_2S_3 . It is known that quasi-1D Sb_2S_3 consists of $[Sb_4S_6]_n$

chains which have five nonequivalent atomic sites, i.e., Sb(1), Sb(2), S(1), S(2) and S(3), as illustrated in Fig. 5a. First principles calculations have shown that Sb_2S_3 involves intricate defect types, including five vacancies ($V_{\text{Sb}(1)}$, $V_{\text{Sb}(2)}$, $V_{\text{S}(1)}$, $V_{\text{S}(2)}$ and $V_{\text{S}(3)}$), five anti-sites ($\text{S}_{\text{Sb}(1)}$, $\text{S}_{\text{Sb}(2)}$, $\text{S}_{\text{S}(1)}$, $\text{S}_{\text{S}(2)}$ and $\text{S}_{\text{S}(3)}$), and twelve interstitials. The interstitials were identified using the Voronoi scheme⁵⁵, despite the material being comprised of only two elemental components^{52, 56, 57}. Our calculation details are provided in Ref.⁵² and the Methods section. The equilibrium defect concentrations as a function of the Sb/S chemical potential are shown in Fig. 5b. Under Sb-rich conditions (i.e., synthesis conditions for control and 4mM-SC Sb_2S_3 devices), S_{S} , V_{S} and V_{Sb} are the most dominant point defects with concentrations higher than 10^{14} cm^{-3} . The corresponding defect levels are shown in Fig. 5c and summarized in Supplementary Table 3. Except for $V_{\text{Sb}(2)}$, most of these defects have traps that match those observed experimentally via DLTS (as indicated by the dashed gray lines). This highlights the challenges in identifying specific defects based solely on defect concentrations or energy levels in Sb_2S_3 . Moreover, our global search reveals that all intrinsic point defects in Sb_2S_3 are amphoteric, exhibiting both donor- and acceptor-like charge states. Therefore, directly comparing experimental defect levels with simulations under the assumption that each defect acts exclusively as a donor or an acceptor may be misleading⁵⁶, since amphoteric defects introduce additional possibilities for matching the measured levels.

While defect formation energies and defect levels calculated from simulations provide insights into the thermodynamic stability, they do not directly account for kinetic factors such as carrier capture processes under real device conditions. Experimental techniques are sensitive to defects that actively capture carriers. To identify the most relevant defects, we first selected those with defect levels and equilibrium concentrations close to the experimental values (Supplementary Table 4), then investigated the potential energy surfaces associated with charge transition processes. Capture cross sections were then calculated for each transition using configuration coordinate (CC) diagrams⁵². The magnitude of the cross sections was used to determine whether each defect predominantly behaves as an electron or a hole

trap. Based on the combined information from defect levels, concentrations, and cross sections, $V_{S(3)}$ and $Sb_{S(2)}$ were identified as the defects most consistent with the experimental observations, with trap levels located at 0.59 and 0.61 eV above the VBM and calculated capture cross sections of 3.77×10^{-16} and $4.00 \times 10^{-17} \text{ cm}^{-2}$, respectively. However, due to the small differences between these trap levels, it is challenging to unambiguously assign $V_{S(3)}$ and $Sb_{S(2)}$ to H1 and H2. One possible reason for the discrepancy between theoretical predictions and experimental observations is the absence of temperature effects in our electronic structure calculations. In real device conditions, defect occupation probabilities and nonradiative recombination dynamics could be influenced by thermal activation. Such temperature effects can lead to a shift of 0.1-0.2 eV in defect levels, partly accounting for the observed differences⁵⁸. The CC diagrams for $V_{S(3)}$ and $Sb_{S(2)}$ are shown in Fig. 5d, e. A larger displacement along the generalized coordinate Q corresponds to stronger lattice relaxation during the charge transition process. For both defects, the energy barriers for hole capture are very small, and the corresponding phonon wavefunctions of the initial and final states exhibit large overlap. A small capture barrier combined with large phonon overlap greatly enhances the transition probability, leading to large hole capture cross-sections on the order of $10^{-16}\sim 10^{-17} \text{ cm}^2$.

We further predicted the maximum achievable V_{OC} and PCE by accounting for both radiative (band-to-band) and defect-mediated non-radiative recombination processes (Supplementary Fig. 17). A film thickness of 350 nm and optical absorption coefficients simulated from first-principles calculations⁴⁹ (HSE06 functional with a bandgap of 1.79 eV), were used as inputs to ensure a consistent radiative limit for both samples. Under the radiative limit, the calculated V_{OC} is 1.70 V, with a corresponding maximum PCE of 21.98%. Non-radiative recombination losses were assessed based on measured trap levels, trap densities and capture cross sections in control and 4mM-SC Sb_2S_3 devices. Since only hole traps are detected by DLTS, we assume non-radiative recombination in these samples is dominated by hole capture processes (i.e., electron capture coefficients are set infinitely high). For the control sample, the predicted V_{OC} is 1.15 V, corresponding to a PCE of 13.34% and a voltage loss ΔV_{OC} of 0.35 V (defined

as $V_{OC}^{SQ} - V_{OC}$, where V_{OC}^{SQ} is calculated to be around 1.50 V). In contrast, the 4mM-SC sample shows an improved V_{OC} of 1.26 V and a PCE of 14.72%, with a reduced ΔV_{OC} of 0.24 V. These predictions agree well with the observed enhanced performance of the 4mM-SC Sb_2S_3 device, but both samples exhibit significant non-radiative losses compared to the radiative limit, highlighting the role of defect-mediated recombination.

Device physics of planar Sb_2S_3 solar cells

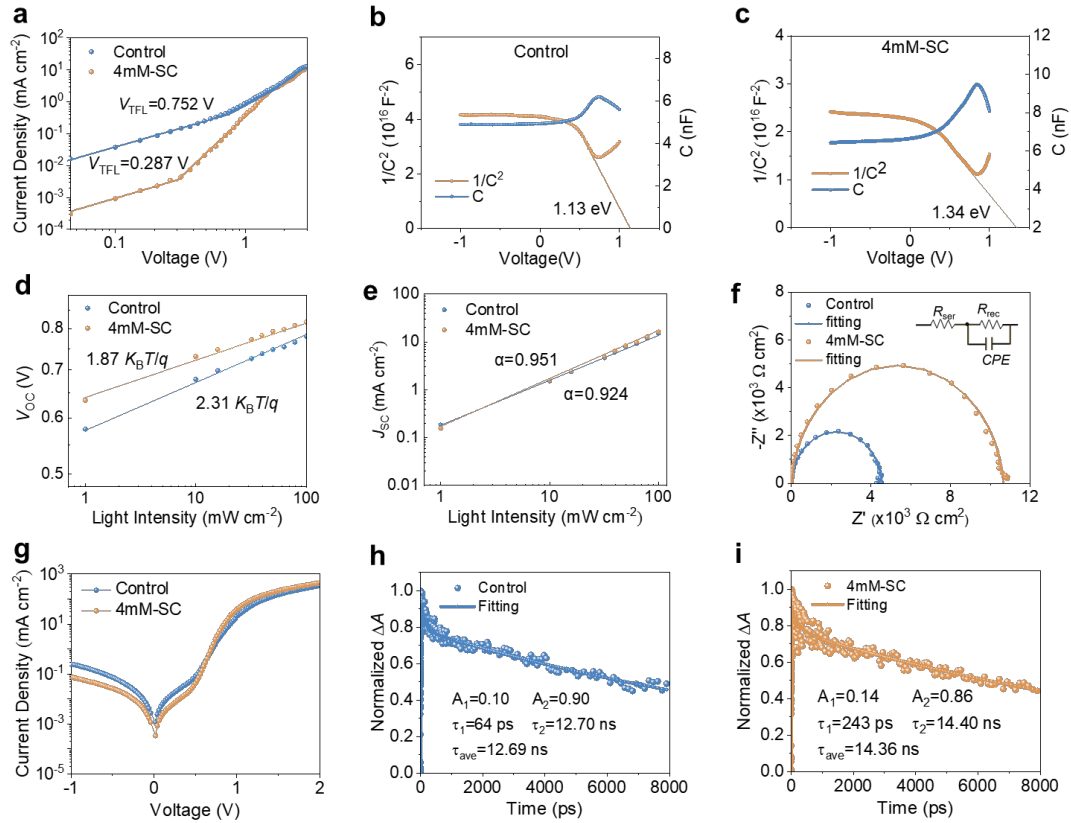


Fig. 6 | Device physics of planar Sb_2S_3 solar cells. **a** Space charge limited current (SCLC) measurements of the control and 4mM-SC devices based on the electron-only device with the configuration of FTO/CdS/ Sb_2S_3 /PCBM/Au. **b,c** Capacitance-voltage ($C-V$) and corresponding Mott-Schottky ($1/C^2 \sim V$) plots of the control and 4mM-SC Sb_2S_3 solar cells measured in the dark. **d,e** Dependences of V_{OC} and J_{SC} on the light intensity for the control and 4mM-SC Sb_2S_3 solar cells. **f** Nyquist plots for the control and 4mM-SC devices measured in the dark, with the equivalent circuit used for fitting shown in the inset. **g** $J-V$ curves measured in the dark for the control and 4mM-SC Sb_2S_3 solar cells. **h,i** Photoinduced absorption (PIA) kinetics (scatter) measurements monitored at 560 nm from transient absorption spectroscopy, along with phenomenological biexponential curve

fits (solid line) for the of the control and 4mM-SC Sb_2S_3 films. Excitation was with a 400 nm wavelength pulsed laser at a repetition rate of 1000 Hz. ΔA is defined as the change in the absorption of the sample before and after pumping.

We further investigate the device physics of Sb_2S_3 solar cells to fully understand underlying mechanism of performance enhancements. The space charge limited current density (SCLC) measurements by the dark logarithmic J - V curves of the electron-only device FTO/CdS/ Sb_2S_3 /PCBM/Au is given in Fig. 6a. At the low voltage Ohmic region, the curve is generally linear. When the voltage exceeds the trap-filled limiting region, the current increases dramatically, implying that the injected carriers have completely occupied the trap states²⁵. The trap-filled limiting voltage (V_{TFL}) values for the control and 4mM-SC device are estimated to be 0.287 V and 0.752 V, respectively. The trap state density (n_{t}) of Sb_2S_3 films can be evaluated according to the equation $V_{\text{TFL}} = qn_{\text{t}}L^2/2\epsilon_{\text{r}}\epsilon_0$, where q is the elementary charge, n_{t} is the trap state density, L is the thickness of the absorber film (here 506 nm and 318 nm for the control and 4mM-SC Sb_2S_3 films, respectively), ϵ_0 is the vacuum permittivity (8.85×10^{-12} F m⁻¹), and ϵ_{r} is the relative permittivity of Sb_2S_3 (6.67 for static dielectric constant)⁵⁹. As a result, the trap state densities for the control and 4mM-SC device are estimated to be 2.17×10^{15} cm⁻³ and 2.12×10^{15} cm⁻³, respectively. The overall reduction in trap state density is consistent with the reduction in GB density, and the order of magnitude of the trap density is consistent with DLTS measurements.

Fig. 6b, c shows the capacitance-voltage (C - V) and corresponding Mott-Schottky ($1/C^2 \sim V$) plots of the control and 4mM-SC Sb_2S_3 devices measured in the dark. It is demonstrated that the abrupt p-n junction capacitance can be expressed using a parallel-plate capacitor model, in which the relationship between the capacitance and the bias voltage is described as $1/C^2 = 2(V_{\text{bi}} - V)/q\epsilon_0\epsilon_{\text{r}}A^2N_{\text{CV}}^{27}$, where q is the elementary charge (1.60×10^{-19} C), ϵ_0 is the vacuum permittivity (8.85×10^{-12} F m⁻¹), ϵ_{r} is the relative permittivity of Sb_2S_3 (6.67), A is the active area of solar cells (0.06 cm²), V_{bi} is the built-in potential, and N_{CV} is the charge-carrier density. According to this equation, the V_{bi} of the 4mM-SC device is calculated to be 1.34 V, larger than that of the control device

(1.13 V). The increase in the V_{bi} reflects the enhanced band bending at the heterointerface, which facilitates the charge separation and reduces the interface recombination. A larger V_{bi} of the depletion region contributes to the enhanced V_{OC} , consistent with the results from J - V curves.

The dependences of V_{OC} and J_{SC} on the light intensity for both solar cells were performed to reveal trap-assisted charge recombination loss mechanisms, as shown in Fig. 6d, e. The relationship between V_{OC} (and J_{SC}) and the light intensity I can be described by $V_{OC} \propto (nk_B T/q) \ln(I)$ and $J_{SC} \propto I^\alpha$, where k_B is the Boltzmann constant, T is the absolute temperature, q is the elementary charge, and α and n reflect the level of charge-carrier recombination^{60, 61, 62}. Under the open-circuit condition, all photogenerated charge-carriers recombine. For ideal trap-free solar cells, the slope of V_{OC} versus $\ln(I)$ is $k_B T/q$. As revealed, the slopes for the control and 4mM-SC devices are linearly fitted to be $2.31k_B T/q$ and $1.87k_B T/q$, respectively. The reduced slope for the 4mM-SC device reflects the suppression of trap-assisted charge-carrier recombination. The parameter α ideally equals 1, and $\alpha < 1$ suggests the loss of photogenerated charge-carriers caused by the incomplete collection. The α values for the control and 4mM-SC devices are estimated to be 0.924 and 0.951, respectively. The increase in α for the 4mM-SC device implies the enhancement of the carrier collection rate⁶². Impedance spectroscopy analysis, Fig. 6f and Supplementary Table 5, shows the 4mM-SC device delivers an increased recombination resistance at the CdS/Sb₂S₃ interface ($R_{rec}=10.66 \text{ k}\Omega \text{ cm}^{-2}$) compared to the control device ($R_{rec}=4.51 \text{ k}\Omega \text{ cm}^{-2}$). The increase in the resistance is suggested to suppress the charge recombination and improve the charge collection in solar cells.

Fig. 6g presents J - V curves of the control and 4mM-SC devices measured under dark conditions. According to the abrupt junction J - V equation and its formula manipulation, the parameters of junction ideality factor (A), the reverse saturation current density (J_0), the series resistance (R_S), and the shunt conductance (G , i.e., $1/R_{SH}$) can be extracted (Supplementary Fig. 18)⁶¹. The detailed analysis is given in Supplementary Note 3. It can be seen that, compared to the control device, the 4mM-SC device has lower R_S and G , which implies an improvement in the carrier extraction

capability. The A values extracted from the control and 4mM-SC devices are 2.38 and 1.91, respectively; the reduced A value indicates the suppression of defect states in the absorber films⁶¹. The calculated J_0 is reduced from 3.22×10^{-5} mA cm⁻² for the control device to 2.09×10^{-6} mA cm⁻² for the 4mM-SC device. The main reason for the generation of J_0 is the charge-carrier recombination caused by deep-level defects in the devices, and thus the reduced J_0 implies the suppression of the defect-induced recombination, contributing to the V_{OC} increase for the 4mM-SC device⁶³.

Ultrafast transient absorption (TA) spectroscopy analysis was further performed to understand the charge-carrier kinetics of FTO/SnO₂/CdS/Sb₂S₃ films. The TA spectra of both the control sample and the 4mM-SC sample (Supplementary Fig. 19a, b) display distinct negative differential absorbance (ground state bleach (GSB) peaks), as well as regions of positive differential absorbance (photoinduced absorption (PIA) peaks). The GSB peaks observed at the wavelengths of 460-520 nm and 610-680 nm can be ascribed to the state filling of CdS and the ground state absorption of Sb₂S₃, respectively. The PIA peak at the wavelength of 520 to 610 nm can be assigned to the formation of sulfide radicals ($S^{\bullet-}$) as a result of the localization of photogenerated holes on the S atom within the Sb₂S₃ lattice^{6, 14, 64}. The transient kinetic decays monitored at 560 nm for both the control and 4mM-SC films can be extracted from the pseudocolor images for the TA spectra of both samples (Supplementary Fig. 19c, d), as presented in Fig. 6h, i. The transient dynamics are well fitted with a phenomenological biexponential model in order to quantitatively compare between samples. The gradual decrease of the PIA peak can be attributed to the decay of trapped holes, i.e., the $S^{\bullet-}$ species, which we here attribute to the nonradiative carrier recombination in Sb₂S₃ films. The 4mM-SC sample delivers higher average time constant (τ_{av}) values (6.61 ns) compared to the control sample (4.93 ns). Such lifetime values lies within the range of 5~60 ns that are commonly reported for antimony chalcogenides³¹. In general, the charge-carrier lifetime of the absorber material is inversely proportional to reverse saturation current density of the device. Hence, a long carrier lifetime is the prerequisite for achieving high V_{OC} of solar cells.

Discussion

While it has been suggested that the low V_{OC} of Sb_2S_3 solar cells is an intrinsic limit caused by self-trapping in the bulk material, we have succeeded in overcoming the predicted 800 mV barrier. This achievement was realized through the formation of large-grained thin films by adding SC to the CBD precursor solution. The growth of high-quality uniform films produces Sb_2S_3 solar cells with PCE of 7.67% under one-sun illumination and a record V_{OC} of 824 mV. Defect characterization and computations reveal that the reduced defect activity in Sb_2S_3 films contribute to the increase in device V_{OC} . We conclude that antimony chalcogenides have the potential to be used in high-performance optoelectronic devices. While intrinsic defects do give rise to non-radiative recombination of photogenerated charge carriers, there is plenty of scope to further increase the performance of this technology through effective defect engineering and crystal growth strategies.

Acknowledgements

J.Z., X.W. and T.S. contributed equally to this work. The financial support by the National Natural Science Foundation of China (nos. 52371219 and W2421064) and the Fundamental Research Funds for the Central Universities (no. JZ2024HGTG0295) is greatly acknowledged. J. Y. and R. L. Z. H. thank UK Research and Innovation for funding through a Frontier Grant (no. EP/X029900/1), awarded via the 2021 ERC Starting Grant scheme. They also thank St. John's College Oxford for funding through the Large Grant scheme. R. L. Z. H. thanks the Royal Academy of Engineering and Science & Technology Facilities Council for funding through a Senior Research Fellowship (no. RCSR2324-18-68). R. Z. and R. L. Z. H. thank the Royal Society for funding (no. IEC/NSFC/242353).

Author contributions

R.Z. and J.Z. designed the experiments and analyzed the data, and also conceived of the idea for this manuscript. J.Z. and T.S. carried out the experiments, device optimizations and data analysis. X.W. carried out the computations. L.W., J.Y., Z.L., A.W., R.L.Z.H. and R.Z. assisted in experiments and data analysis. R.Z., J.Z., X.W., A.W. and R.L.Z.H., wrote the manuscript. All authors commented on the manuscript.

Conflict of interest

The authors declare no competing interests.

Supplementary Materials

The online version contains supplementary materials available at xxx

References and Notes

1. Polman, A., Knight, M., Garnett, E. C., Ehrler, B. & Sinke, W. C. Photovoltaic materials: Present efficiencies and future challenges. *Science* **352**, 4424 (2016).
2. Blakesley, J. C. et al. Roadmap on established and emerging photovoltaics for sustainable energy conversion. *J. Phys. Energy* **6**, 041501 (2024).
3. <https://www.nrel.gov/pv/cell-efficiency.html>.
4. Wang, S. et al. A novel multi-sulfur source collaborative chemical bath deposition technology enables 8%-efficiency Sb₂S₃ planar solar cells. *Adv. Mater.* **34**, 2206242 (2022).
5. Duan, Z. et al. Sb₂Se₃ thin-film solar cells exceeding 10% power conversion efficiency enabled by injection vapor deposition technology. *Adv. Mater.* **34**, 2202969 (2022).
6. Tang, R. et al. Hydrothermal deposition of antimony selenosulfide thin films enables solar cells with 10% efficiency. *Nat. Energy* **5**, 587-595 (2020).
7. Zhao, Y. et al. Regulating deposition kinetics via a novel additive-assisted chemical bath deposition technology enables fabrication of 10.57%-efficiency Sb₂Se₃ solar cells. *Energ. Environ. Sci.* **15**, 5118-5128 (2022).
8. Green, M. et al. Solar cell efficiency tables (version 57). *Prog. photovolt.* **29**, 3-15 (2021).
9. Chen, P. et al. Multifunctional ytterbium oxide buffer for perovskite solar cells. *Nature* **625**, 516-522 (2024).
10. Wang, A., He, M., Green, M. A., Sun, K. & Hao, X. A critical review on the progress of kesterite solar cells: Current strategies and insights. *Adv. Energy Mater.* **13**, 2203046 (2023).
11. Green, M. A. & Bremner, SP. Energy conversion approaches and materials for high-efficiency photovoltaics. *Nat. Mater.* **16**, 23-34 (2017).

12. Fu, Y. et al. Structural and electronic features enabling delocalized charge-carriers in CuSbSe. *Nat. Commun.* **16**, 65 (2025).
13. Chen, X. et al. Solvent-assisted hydrothermal deposition approach for highly-efficient Sb₂(S,Se)₃ thin-film solar cells. *Adv. Energy Mater.* **13**, 2300391 (2023).
14. Liu, X. N. et al. Grain engineering of Sb₂S₃ thin films to enable efficient planar solar cells with high open-circuit voltage. *Adv. Mater.* **36**, 2305841 (2024).
15. Chen, J. W. et al. Recent advances and prospects of solution-processed efficient Sb₂S₃ solar cells. *Adv. Funct. Mater.* **34**, 2313676 (2024).
16. Mao, X. L. et al. Ultrathin SnO₂ buffer layer aids in interface and band engineering for Sb₂(S,Se)₃ solar cells with over 8% efficiency. *ACS Appl. Energy Mater.* **5**, 3022-3033 (2022).
17. Hadke, S. et al. Emerging chalcogenide thin films for solar energy harvesting devices. *Chem. Rev.* **122**, 10170-10265 (2021).
18. Lei, H., Chen, J., Tan, Z. & Fang, G. Review of recent progress in antimony chalcogenide-based solar cells: Materials and devices. *Sol. RRL* **3**, 1900026 (2019).
19. Dong, J. B. et al. Carrier management through electrode and electron-selective layer engineering for 10.70% efficiency antimony selenosulfide solar cells. *Nat. Energy* **10**, 1-12 (2025).
20. Chen, S. et al. A codoping strategy for efficient planar heterojunction Sb₂S₃ solar cells. *Adv. Energy Mater.* **12**, 2202897 (2022).
21. Pecunia, V., Occhipinti, L. G. & Hoyer, R. L. Z. Emerging indoor photovoltaic technologies for sustainable internet of things. *Adv. Energy Mater.* **11**, 2100698 (2021).
22. Chen, X. et al. Indoor photovoltaic materials and devices for self-powered internet of things applications. *Mater. Today Energy* **44**, 101621 (2024).
23. Kondrotas, R., Chen, C. & Tang, J. Sb₂S₃ solar cells. *Joule* **2**, 857-878 (2018).
24. Rühle, S. Tabulated values of the Shockley-Queisser limit for single junction solar cells. *Sol. Energy* **130**, 139-147 (2016).
25. Zhu, L. X. et al. Parallel planar heterojunction strategy enables Sb₂S₃ solar cells with efficiency exceeding 8%. *Angew. Chem. Int. Edit.* **62**, 202312951 (2023).
26. Green, M. A. et al. Solar cell efficiency tables (version 62). *Prog. Photovol.* **31**, 651-663 (2023).
27. Tang, R. et al. Heterojunction annealing enabling record open-circuit voltage in antimony triselenide solar cells. *Adv. Mater.* **34**, 2109078 (2022).
28. Yang, Z. L. et al. Ultrafast self-trapping of photoexcited carriers sets the upper limit on antimony trisulfide photovoltaic devices. *Nat. Commun.* **10**, 4540 (2019).
29. Tao, W. J. et al. Coupled electronic and anharmonic structural dynamics for carrier self-trapping in photovoltaic antimony chalcogenides. *Adv. Sci.* **9**, 2202154 (2022).
30. Wang, X., Ganose, A. M., Kavanagh, S. R. & Walsh, A. Band versus polaron: Charge transport in antimony chalcogenides. *ACS Energy Lett.* **7**, 2954-2960 (2022).
31. Chen, C. & Tang, J. Open-circuit voltage loss of antimony chalcogenide solar cells: Status, origin, and possible solutions. *Acs Energy Lett.* **5**, 2294-2304 (2020).
32. Peng, X. et al. Negative-pressure sulfurization of antimony sulfide thin films for generating a record open-circuit voltage of 805 mV in solar cell applications. *J. Mater. Chem. A* **11**, 19298-19307 (2023).
33. Chen, X. et al. Additive engineering for Sb₂S₃ indoor photovoltaics with efficiency exceeding 17%. *Light-Sci. Appl.* **13**, 281 (2024).
34. Gao, H. H. et al. Band gap adjustable antimony selenosulfide indoor photovoltaics with 20% efficiency. *Sol. RRL* **8**, 2400389 (2024).

35. Koutsourakis, K. et al. Reaching a consensus on indoor photovoltaics testing. *Joule* **9**, 102127 (2025).
36. G. Krishnamurthy-Grandhi, G. K. et al. Promises and challenges of indoor photovoltaics. *Nat. Rev. Clean Tech.* **1**, 132–147 (2025).
37. Rijal, S. et al. Templated growth and passivation of vertically oriented antimony selenide thin films for high-efficiency solar cells in substrate configuration. *Adv. Funct. Mater.* **32**, 2110032 (2021).
38. Liu, Z. Z., Cao, F. R., Wang, M., Wang, M. & Li, L. Observing the defect passivation of grain boundary with 2-aminoterephthalic acid for efficient and stable perovskite solar cells. *Angew. Chem. Int. Edit.* **59**, 4161-4167 (2020).
39. Jiang, X. et al. Ultra-high open-circuit voltage of tin perovskite solar cells via an electron transporting layer design. *Nat. Commun.* **11**, 1245 (2020).
40. Sengupta, S., Aggarwal, R. & Golan, Y. The effect of complexing agents in chemical solution deposition of metal chalcogenide thin films. *Mater. Chem. Front.* **5**, 2035-2050 (2021).
41. Dunlap-Shohl, W. A., Zhou, Y., Padture, N. P. & Mitzi, D. B. Synthetic approaches for halide perovskite thin films. *Chem. Rev.* **119**, 3193-3295 (2019).
42. Jung, M., Ji, S. G., Kim, G. & Seok, S. I. Perovskite precursor solution chemistry: from fundamentals to photovoltaic applications. *Chem. Soc. Rev.* **48**, 2011-2038 (2019).
43. Si, H. et al. Deciphering the NH_4PbI_3 intermediate phase for simultaneous improvement on nucleation and crystal growth of perovskite. *Adv. Funct. Mater.* **27**, 1701804 (2017).
44. Wang, X. M. et al. Manipulating the electrical properties of $\text{Sb}_2(\text{S,Se})_3$ film for high-efficiency solar cell. *Adv. Energy Mater.* **10**, 2002341 (2020).
45. Agawane, G. L. et al. Non-toxic complexing agent Tri-sodium citrate's effect on chemical bath deposited ZnS thin films and its growth mechanism. *J. Alloy Compd.* **535**, 53-61 (2012).
46. Wen, X. X. et al. Vapor transport deposition of antimony selenide thin film solar cells with 7.6% efficiency. *Nat. Commun.* **9**, 2179 (2018).
47. Heo, S. et al. Deep level trapped defect analysis in $\text{CH}_3\text{NH}_3\text{PbI}_3$ perovskite solar cells by deep level transient spectroscopy. *Energ. Environ. Sci.* **10**, 1128-1133 (2017).
48. Che, B. et al. Thermally driven point defect transformation in antimony selenosulfide photovoltaic materials. *Adv. Mater.* **35**, 2208564 (2023).
49. Wang, X. W., Li, Z. Z., Kavanagh, S. R., Ganose, A. M. & Walsh, A. Lone pair driven anisotropy in antimony chalcogenide semiconductors (vol 24, pg 7195, 2022). *Phys. Chem. Chem. Phys.* **25**, 25055-25055 (2023).
50. Lang, D. V. Deep-level transient spectroscopy: a new method to characterize traps in semiconductors. *J. Appl. Phys.* **45**, 3023–3032 (1974).
51. Szatkowski, J., Sieranski, K., Hajdusianek, A. & Placzek-Popko, E. Deep hole traps in Be-doped $\text{Al}_{0.2}\text{Ga}_{0.8}\text{As}$ layers grown by molecular beam epitaxy. *Physica B* **340**, 345-348 (2003).
52. Wang, X. W., Kavanagh, S. R. & Walsh, A. Sulfur vacancies limit the open-circuit voltage of Sb_2S_3 solar cells. *ACS Energy Lett.* **10**, 161-167 (2024).
53. Seán, R. et al. Doped: Python toolkit for robust and repeatable charged defect supercell calculations. *J. Open Source Softw.* **9**, 6433 (2024).
54. Irea, Mosquera-Lois, S. R. K., Walsh, A. & David, O. Scanlon. ShakeNBreak: Navigating the defect configurational landscape. *J. Open Source Softw.* **7**, 4817 (2022).
55. Goyal, A., Gorai, P., Peng, H. W. & Lany, S. Stevanovic V. A computational framework for automation of point defect calculations. *Comp. Mater. Sci.* **130**, 1-9 (2017).

56. Guo, L. et al. Scalable and efficient Sb₂S₃ thin-film solar cells fabricated by close space sublimation. *APL Mater.* **7**, 041105 (2019).
57. Cai, Z., Dai, C-M. & Chen, S. Intrinsic defect limit to the electrical conductivity and a two-step p-type doping strategy for overcoming the efficiency bottleneck of Sb₂S₃-based solar cells. *Sol. RRL* **4**, 1900503 (2020).
58. Qiao, S. et al. Temperature effect on charge-state transition levels of defects in semiconductors. *Phys. Rev. B* **105**, 115201 (2022).
59. Wang, C. X. et al. Interfacial defect healing of In₂S₃/Sb₂(S,Se)₃ heterojunction solar cells with a novel wide-bandgap InOCl passivator. *J. Mater. Chem. A* **11**, 19914-19924 (2023).
60. Zhou, J. et al. Colloidal SnO₂-assisted CdS electron transport layer enables efficient electron extraction for planar perovskite solar cells. *Sol. RRL* **5**, 2100494 (2021).
61. Zhou, R. et al. Orientation control of close-spaced sublimation processed Sb₂S₃ thin films for efficient and stable planar solar cells. *Appl. Phys. Lett.* **124**, 233903 (2024).
62. Zhou, J. T. et al. Unraveling the roles of mesoporous TiO₂ framework in CH₃NH₃PbI₃ perovskite solar cells. *Sci. China Mater.* **63**, 1151-1162 (2020).
63. Zhou, R. et al. Bulk heterojunction antimony selenosulfide thin-film solar cells with efficient charge extraction and suppressed recombination. *Adv. Funct. Mater.* **34**, 2308021 (2024).
64. Lian, W. et al. Revealing composition and structure dependent deep-level defect in antimony trisulfide photovoltaics. *Nat. Commun.* **12**, 3260 (2021).
65. Kumagai, Y. & Oba, F. Electrostatics-based finite-size corrections for first-principles point defect calculations. *Phys. Rev. B* **89**, 195205 (2014).
66. Stoneham, A. M. Theory of defects in solids. *OUP Oxford, Oxford, 1975*.
67. Alkauskas, A., Yan, Q. M. & Van, de, Walle, C.G. First-principles theory of nonradiative carrier capture via multiphonon emission. *Phys. Rev. B* **90**, 075202 (2014).
68. Kim, S., Márquez, J. A., Unold, T. & Walsh, A. Upper limit to the photovoltaic efficiency of imperfect crystals from first principles. *Energ. Environ. Sci.* **13**, 1481-1491 (2020).
69. Kim, S. & Walsh, A. Ab initio calculation of the detailed balance limit to the photovoltaic efficiency of single p-n junction kesterite solar cells. *Appl. Phys. Lett.* **118**, 243905 (2021).